molecular pharmaceutics

pubs.acs.org/molecularpharmaceutics

Article

Diffusion and Protein Corona Formation of Lipid-Based Nanoparticles in the Vitreous Humor: Profiling and Pharmacokinetic Considerations

Shirin Tavakoli, Otto Kalevi Kari, Tiina Turunen, Tatu Lajunen, Mechthild Schmitt, Julia Lehtinen, Fumitaka Tasaka, Petteri Parkkila, Joseph Ndika, Tapani Viitala, Harri Alenius, Arto Urtti, and Astrid Subrizi*

Cite This: *Mol. Pharmaceutics* 2021, 18, 699–713

Read Online

ACCESS | Metrics & More | Article Recommendations | Supporting Information

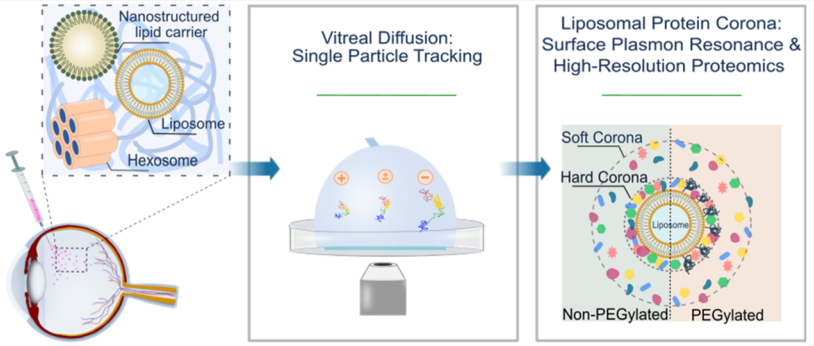

ABSTRACT: The vitreous humor is the first barrier encountered by intravitreally injected nanoparticles. Lipid-based nanoparticles in the vitreous are studied by evaluating their diffusion with single-particle tracking technology and by characterizing their protein coronae with surface plasmon resonance and high-resolution proteomics. Single-particle tracking results indicate that the vitreal mobility of the formulations is dependent on their charge. Anionic and neutral formulations are mobile, whereas larger (>200 nm) neutral particles have restricted diffusion, and cationic particles are immobilized in the vitreous. PEGylation increases the mobility of cationic and larger neutral formulations but does not affect anionic and smaller neutral particles. Convection has a significant role in the pharmacokinetics of nanoparticles, whereas diffusion drives the transport of antibodies. Surface plasmon resonance studies determine that the vitreal corona of anionic formulations is sparse. Proteomics data reveals 76 differentially abundant proteins, whose enrichment is specific to either the hard or the soft corona. PEGylation does not affect protein enrichment. This suggests that protein-specific rather than formulation-specific factors are drivers of protein adsorption on nanoparticles in the vitreous. In summary, our findings contribute to understanding the pharmacokinetics of nanoparticles in the vitreous and help advance the development of nanoparticle-based treatments for eye diseases.

KEYWORDS: *lipid-based nanoparticle, ocular pharmacokinetics, vitreal diffusion, protein corona, single-particle tracking, proteomics*

1. INTRODUCTION

Eye disorders affecting the retina are major causes of visual impairment and blindness, and their prevalence is increasing as a result of population aging. The pharmacological treatment of posterior segment disorders, such as age-related macular degeneration and diabetic retinopathy, is challenging because tight blood–ocular barriers effectively prevent the delivery of therapeutic agents to the target tissues.[1] For this reason, drugs must be injected directly into the eye (intravitreal injections) to achieve therapeutic concentrations in the retina. Other administration routes such as subconjunctival or suprachoroidal injections and systemic administration are being studied, but are not yet viable clinical options.[1] Intravitreal injections offer several advantages, including the achievement of therapeutic intraocular drug concentrations immediately after injection, bypass of blood–ocular barriers, and avoidance of systemic toxicity. Nevertheless, a small number of patients experience severe, vision-threatening complications after intravitreal injection. In addition, repeated injections needed in the treatment of chronic ocular diseases pose a considerable

Special Issue: Nanomedicines Beyond Cancer

Received: April 17, 2020
Revised: June 18, 2020
Accepted: June 25, 2020
Published: June 25, 2020

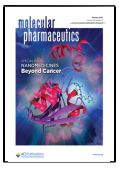

https://dx.doi.org/10.1021/acs.molpharmaceut.0c00411
Mol. Pharmaceutics 2021, 18, 699–713

Table 1. Lipid Composition and Physicochemical Characteristics of Lipid-Based Nanoparticles[a]

formulation		lipid composition	molar ratio [mol%]	size [nm]	PdI	ζ potential [mV]
		<50 nm, Light-Activated Liposome and Control Liposomes				
anionic	AL1-PEG	DPPC:DSPG: Lyso-PC:DSPC:DSPE-PEG:ICG	75:10:10:5:4:2	51.0	0.144	−28.1
	AL2	DPPC:DSPG:Lyso-PC:DSPC:DSPE:ICG	75:10:10:5:4:2	46.7	0.219	−38.0
	AL3-PEG	DPPC:DSPG: Lyso-PC:DSPC:DSPE-PEG	75:10:10:5:4	39.2	0.145	−20.9
	AL4	DPPC:DSPG:Lyso-PC:DSPC:DSPE	75:10:10:5:4	48.7	0.145	−40.8
neutral	NL1-PEG	DPPC:DSPC:Lyso-PC:DSPE-PEG:ICG	75:15:10:4:2	48.9	0.216	−1.7
	NL2	DPPC:DSPC:Lyso-PC:DSPE:ICG	75:15:10:4:2	46.3	0.195	−6.7
	NL3-PEG	DPPC:DSPC:Lyso-PC:DSPE-PEG	75:15:10:4	46.9	0.224	−1.4
	NL4	DPPC:DSPC:Lyso-PC:DSPE	75:15:10:4	35.7	0.314	−1.5
cationic	CL1-PEG	DPPC:DOTAP:Lyso-PC:DSPC:DSPE-PEG:ICG	75:10:10:5:4:2	43.0	0.072	17.7
	CL2	DPPC:DOTAP:DSPC:Lyso-PC:DSPE:ICG	75:10:10:5:4:2	46.5	0.216	29.4
	CL3-PEG	DPPC:DOTAP:Lyso-PC:DSPC:DSPE-PEG	75:10:10:5:4	42.6	0.312	15.7
	CL4	DPPC:DOTAP:DSPC:Lyso-PC:DSPE	75:10:10:5:4	49.9	0.294	32.5
		100−200 nm, Light-Activated Liposome and Control Liposomes				
anionic	AL5-PEG	DPPC:DSPG: Lyso-PC:DSPC:DSPE-PEG:ICG	75:10:10:5:4:2	104.3	0.075	−18.5
	AL6	DPPC:DSPG:Lyso-PC:DSPC:DSPE:ICG	75:10:10:5:4:2	105.2	0.053	−56.3
	AL7-PEG	DPPC:DSPG: Lyso-PC:DSPC:DSPE-PEG	75:10:10:5:4	107.1	0.066	−22.8
	AL8	DPPC:DSPG:Lyso-PC:DSPC:DSPE	75:10:10:5:4	119.8	0.023	−50.6
neutral	NL5-PEG	DPPC:DSPC:Lyso-PC:DSPE-PEG:ICG	75:15:10:4:2	107.6	0.086	−3.6
	NL6	DPPC:DSPC:Lyso-PC:DSPE:ICG	75:15:10:4:2	125.8	0.035	−7.2
	NL7-PEG	DPPC:DSPC:Lyso-PC:DSPE-PEG	75:15:10:4	110.8	0.092	−1.2
	NL8	DPPC:DSPC:Lyso-PC:DSPE	75:15:10:4	110.6	0.097	−7.1
cationic	CL5-PEG	DPPC:DOTAP:Lyso-PC:DSPC:DSPE-PEG:ICG	75:10:10:5:4:2	110.8	0.092	18.2
	CL6	DPPC:DOTAP:DSPC:Lyso-PC:DSPE:ICG	75:10:10:5:4:2	112.6	0.056	33.1
	CL7-PEG	DPPC:DOTAP:Lyso-PC:DSPC:DSPE-PEG	75:10:10:5:4	111.6	0.082	14.0
	CL8	DPPC:DOTAP:DSPC:Lyso-PC:DSPE	75:10:10:5:4	100.3	0.056	31.7
		>200 nm, Light-Activated Liposome and Control Liposomes				
anionic	AL9-PEG	DPPC:DSPG: Lyso-PC:DSPC:DSPE-PEG:ICG	75:10:10:5:4:2	208.8	0.122	−38.8
	AL10	DPPC:DSPG:Lyso-PC:DSPC:DSPE:ICG	75:10:10:5:4:2	212.1	0.052	−57.1
	AL11-PEG	DPPC:DSPG: Lyso-PC:DSPC:DSPE-PEG	75:10:10:5:4	291.8	0.131	−30.8
	AL12	DPPC:DSPG:Lyso-PC:DSPC:DSPE	75:10:10:5:4	291.8	0.084	−55.4
neutral	NL9-PEG	DPPC:DSPC:Lyso-PC:DSPE-PEG:ICG	75:15:10:4:2	224.4	0.121	−1.4
	NL10	DPPC:DSPC:Lyso-PC:DSPE:ICG	75:15:10:4:2	254.4	0.86	−6.8
	NL11-PEG	DPPC:DSPC:Lyso-PC:DSPE-PEG	75:15:10:4	270.6	0.071	−1.2
	NL12	DPPC:DSPC:Lyso-PC:DSPE	75:15:10:4	227.3	0.34	−9.6
cationic	CL9-PEG	DPPC:DOTAP:Lyso-PC:DSPC:DSPE-PEG:ICG	75:10:10:5:4:2	251.2	0.115	18.3
	CL10	DPPC:DOTAP:DSPC:Lyso-PC:DSPE:ICG	75:10:10:5:4:2	236.1	0.102	41.0
	CL11-PEG	DPPC:DOTAP:Lyso-PC:DSPC:DSPE-PEG	75:10:10:5:4	267.9	0.125	14.4
	CL12	DPPC:DOTAP:DSPC:Lyso-PC:DSPE	75:10:10:5:4	202.9	0.315	33.9
		Rigid-Membrane Liposomes				
anionic	AR1	DSPC:DSPG:CHOL	50:10:40	142.0	0.072	−53.0
	AR2	DSPC:DSPG:CHOL	57.5:2.5:40	139.0	0.074	−43.0
neutral	NR1	DSPC:CHOL	60:40	180.0	0.097	−10.0
cationic	CR1	DSPC:DOTAP:CHOL	50: 10: 40	139.0	0.065	43.0
	CR2-PEG	DSPC:DOTAP:CHOL:DSPE-PEG	55:10:32.5:2.5	134.0	0.050	30.0
		Hexosome				
neutral	NH	DOPC:VE	70:30	300.0	0.15	
		Nanostructured Lipid Carriers (NLCs)				
neutral	NN	Compritol 888 ATO:Miglyol 812	51.5:48.5	152.0	0.10	−11.8
	NN-PEG	Compritol 888 ATO:Miglyol 812:DSPE-PEG	51.4:48.3:0.3	150.0	0.14	−10.1

[a]Abbreviations: (L) light-activated liposomes, (R) rigid-membrane liposomes, (H) hexosomes, and (N) NLCs. The formulations are divided based on charge ((A) anionic, (N) neutral, (C) cationic) and on size. Based on this nomenclature, for example, AL indicates an anionic light-activated liposome formulation.

burden to patients, increase the strain on medical personnel, and raise the costs of public healthcare.

Nanoparticles may increase ocular drug bioavailability, retention time in ocular tissues, efficacy, patient comfort, and compliance and minimize adverse drug reactions. Nanoparticles are especially important for the delivery of small regulatory RNAs, proteins, and peptides that require intracellular delivery into retinal cells. If nanoparticles are to be injected into the vitreous, then it is of paramount importance to study their diffusion properties as well as their binding interactions within the vitreous gel. The vitreous is a highly hydrated gel-like matrix (more than 98% water) composed

https://dx.doi.org/10.1021/acs.molpharmaceut.0c00411
Mol. Pharmaceutics 2021, 18, 699−713

mainly of collagen fibers and glycosaminoglycans (mostly hyaluronan, some heparan sulfate, and chondroitin sulfate) that confer its characteristic polyanionic nature.[2,3] Pitkänen and colleagues first recognized that the vitreous poses a substantial barrier to nonviral gene delivery systems.[4] Soon after, Peeters et al. found that the vitreous permits free mobility to PEGylated particles smaller than 500 nm.[5] Later, single-particle tracking technology allowed the measurement of the diffusion coefficients of nanoparticles in intact vitreous.[6,7] According to Xu's estimates, the average mesh size of fresh bovine vitreous is about 550 nm. Moreover, they found that cationic particles of any size are immobilized in the vitreous humor by electrostatic interactions with negatively charged hyaluronic acid molecules.[6]

Aside from diffusion, intravitreal protein binding may be another important factor that significantly alters the vitreal pharmacokinetics of nanoparticles. Recently, coadministration of a 40 kDa nanobody with albumin led to a 3-fold increased vitreous half-life in rabbits,[8] whereas protein binding only had a modest influence on the vitreal half-life of 35 small molecule drugs.[9] The extent of intravitreal protein binding on nanoparticles has not been studied, even though the "protein corona" influences the biodistribution of systemic nanoparticles,[10] and the vitreous proteome is more diverse and biologically active than previously known.[11] No studies have been published on the vitreal corona of liposomal systems, which are still the most common types of nanomaterial containing drug products evaluated by the Food and Drug Administration.[12]

In this study, we employed single-particle tracking technology to evaluate the intravitreal diffusion of a variety of lipid-based formulations, including near-infrared light-activated liposomes, which we previously showed to enable temporal and spatial control of drug release that is based on incorporation of FDA-approved dye, indocyanine green (ICG), in the liposomes.[13,14] Other formulations included rigid-membrane liposomes, hexosomes, and nanostructured lipid carriers. Moreover, we studied the effect of PEGylation on vitreal protein binding in anionic light-activated liposome formulations and its influence on the composition of the hard and soft coronae in the liquefied porcine vitreous with surface plasmon resonance and high-resolution proteomics using a method that we published recently.[15] We analyzed the biological functions of the most enriched proteins in both corona subsections to explore the possible biological interactions.

2. EXPERIMENTAL SECTION

2.1. Materials. 1,2-Distearoyl-sn-glycero-3-phosphoglycerol (DSPG), 1,2-dipalmitoyl-*sn*-glycero-3-phosphocholine (DPPC), 1,2-distearoyl-sn-glycero-3-phosphocholine (DSPC), 1-stearoyl-2-hydroxy-*sn*-glycero-3-phosphocholine (Lyso PC), 1,2-distearoyl-*sn*-glycero-3 phosphoethanolamine (DSPE), 1,2-distearoyl-*sn*-glycero-3-phosphoethanolamine-*N*-[methoxy-(polyethylene glycol)-2000] (DSPE-PEG), 1,2-dioleoyl-3-trimethylammonium-propane (DOTAP), 1,2-dipalmitoyl-*sn*-glycero-3-phosphoethanolamine-*N*-(lissamine rhodamine B sulfonyl) (Liss Rhod-PE), nonlabeled cholesterol, and labeled cholesterol (23-(dipyrromethaneboron difluoride)-24-norcholesterol) were purchased from Avanti Polar Lipids, Inc. (Alabaster, AL, USA). 1,2-Dioleoyl-*sn*-glycero-3-phosphocholine (DOPC) was purchased from NOF Corporation (Tokyo, Japan). All lipids were used without further purification. The extruder was from Avanti Polar Lipids (Alabaster, AL, USA) and the 30, 50, 100, 200, 400, and 800 nm Nuclepore polycarbonate membranes (diameter 19 mm) were from Whatman Int. Ltd. (Maidstone, England). Dimethyl acetamide (DMA), vitamin E (α-tocopherol), and glycerol were from Fluka (Buchs, Switzerland). Compritol 888 ATO and Miglyol 812 were gifts from Gattefosse (Saint-Priest, France) and Cremer Oleo GmbH (Hamburg, Germany), respectively. Chloroform and methanol used in the lipid stock solutions, HEPES (4-(2-hydroxyethyl) piperazine-1-ethanesulfonic acid), Kolliphor EL (CO35), Nile Red (NR), stearylamine (SA), benzalkonium chloride (BAK), benzyldimethylhexadecyl-ammonium chloride (CKC), *N*,*N*-dimethyl sulfoxide (DMSO), and PBS tablets were purchased from Sigma-Aldrich (St. Louis, MO, USA). All reagents were analytical grade.

2.2. Preparation of Light-Activated Liposomes. Liposomes were formed by a thin film hydration method, as described previously.[13] Briefly, lipids (10 μmol) were dissolved in chloroform at various molar ratios (Table 1); then, the chloroform was evaporated at 65 °C under a nitrogen flow by gradually reducing the pressure to 70 mbar over 40 min. The thin lipid layer was hydrated with HEPES buffer saline (500 μL, 20 mM HEPES and 140 mM NaCl, pH 7.4) in a 65 °C water bath. The formed liposomes were extruded 11 times at the same temperature through a polycarbonate membrane with pores of 30, 50, 100, 200, and 400 nm with a syringe-type mini-extruder. Thereafter, the formulation was quickly cooled and stored at 4 °C. Anionic and cationic formulations were made using DSPG and DOTAP, respectively, at the final molar ratio of 10%, which was replaced partially with DSPC. PEGylated liposomes were prepared with PEG-2000 (4 mol %), which is at the intersection of the mushroom and brush configurations but retains good bilayer stability.[16−18] These liposome formulations have also demonstrated good stability in serum and vitreous.[18] Liss Rhod-PE (0.3 mol%) was applied to label the liposomes. To integrate the Indocyanine Green (ICG, 0.2 μmol) into the lipid bilayers, ICG was dissolved in methanol and added to the lipid mixture in chloroform prior to evaporation of the organic solvent.

2.3. Preparation of Rigid-Membrane Liposomes. Liposomes were prepared as in section 2.2. The formed liposomes were sonicated for 4 min and then extruded 15 times through a 200 nm pore size stacked polycarbonate membrane. Liposomes were kept at 4 °C until analysis. PEGylated liposomes were prepared to mask the charged lipids, by replacing a part of the cholesterol (8 mol%) with DSPE-PEG at different molar ratios. To label the liposomes, labeled cholesterol (BDP-chol, 1 mol%) was added.

2.4. Preparation of Hexosomes. The lipid components, DOPC and vitamin E (α-tocopherol, VE), were weighed into a glass vial at a ratio of 70:30 w/w % (Table 1). The lipophilic dye Nile Red was dissolved in DMA and added to the lipid mix (final concentration 0.01−0.02%). A homogeneous solution was obtained by stirring the mixture for 1 h at 70 °C on a hot plate magnet stirrer. The stabilizers Pluronic F127 (0.5%) and Tween 80 (0.5%) were dissolved in either PBS or glycerol (2.5%)-containing deionized water solution. The Nile Red-containing lipid mixture was then transferred to another glass vial and heated to 90 °C. One-third of the preheated (90 °C) stabilizer-containing aqueous solution was added to the mixture, stirred for 30 min, and sonicated for 15 min using a tip sonicator without a pulse at an amplitude of 40%. Next, the other two-thirds of the preheated aqueous phase were added

https://dx.doi.org/10.1021/acs.molpharmaceut.0c00411
Mol. Pharmaceutics 2021, 18, 699−713

and tip sonicated for 45 min under the same conditions, resulting in a homogeneous hexosome solution (100 mg mL^{-1} lipid). Hexosomes were stored for up to 2 weeks at room temperature.

2.5. Preparation of Nanostructured Lipid Carriers (NLC). Appropriate amounts of lipid solutions in chloroform were pipetted into a glass vial (Table 1). The chloroform was evaporated with a stream of nitrogen gas. Compritol 888 ATO, Nile Red, and CKC were weighed and added to the mixture. Miglyol 812 was weighed and added. The lipids were melted on a hot plate (150 °C), while stirring with a magnet bar (1000 rpm) for 3 min. Appropriate volumes of prewarmed (~80−90 °C) PBS or glycerol (2−2.6%) aqueous solution with Kolliphore EL (3%, PEG-35 castor oil) were added to the lipid mixture while stirring. Then, the mixture was stirred for further 3 min, sonicated for 10−30 min at 80−85 °C, and swirled occasionally to obtain a homogeneous emulsion (10% w/v). The mixture was stirred on ice for 30 min and then at room temperature for 60−90 min. NLCs were stored at 4 °C.

2.6. Particle Size and ζ Potential. The particle size was determined by dynamic light scattering (DLS) using a Malvern Zetasizer APS (Malvern Instruments Ltd., Malvern, United Kingdom) system. Malvern DTS v7.01 software was used for data acquisition, and results were reported as size distributions by particle numbers with a polydispersity index (PdI). Each sample was diluted at a 1:10 v/v ratio and measured three times with 13 subruns. Samples were measured at room temperature. The ζ potential was measured with the same dilution ratio at room temperature using a Zetasizer ZS v7.1.1 (Malvern Instruments Ltd.).

2.7. Preparation of Intact Porcine Vitreous Samples. Fresh porcine eyes were provided by a local slaughterhouse (HKScan Finland Oyj, Forssa, Finland). Enucleation was done by a transconjunctival incision 15 min after sacrificing the animal, and the eyes were kept on ice during transport. Extraocular tissues were removed, followed by their short immersion into 70% ethanol. The eyes were then kept in PBS at 4 °C overnight before dissection. To study the intact porcine vitreous, we followed a modified procedure from Xu and colleagues.[6] Briefly, the anterior part of the eye, including the lens, was removed, leaving the intact vitreous exposed. Fluorescently labeled particles (50 μL) were injected into the vitreous using a 30 G BD Micro-Fine+ insulin syringe (BD, Franklin Lakes, NJ, USA). The particle concentrations were 0.25 mg mL^{-1} (0.025%) for light-activated liposomes, 0.16−0.34 mg mL^{-1} for rigid-membrane liposomes, 100 mg mL^{-1} for hexosomes, and 10 mg mL^{-1} for NLCs. The injection was done in the center of the eye cup perpendicularly to the cut surface and at a depth of 0.5 cm. Then a 35 mm microwell dish having a 14 mm diameter glass window at the bottom (MatTek Corporation, Ashland, MA, USA) was placed on top of the cut eyeball, and the dish was inverted. The edges of the eye were fixed with Loctite Precision super glue (Henkel Corp., NJ, USA).

2.8. Nanoparticle Visualization and Tracking Analysis with Imaris Software. The movement of the labeled particles was recorded with an Andor Neo sCMOS camera mounted on a spinning disk confocal microscope (3i Marianas, Intelligent Imaging Innovations, Denver, CO, USA) equipped with a temperature control system. The particles were observed using either a 20×/0.4 LD Plan-Neofluar Ph2 Corr WD = 7.9 M27 long distance objective, a 20×/0.8 Plan-Apochromat Ph2 WD = 0.55 M27 objective, or a 63×/1.2 W C-Apochromat Corr WD = 0.28 M27 objective. A blue (488 nm, 50 mW) solid-state laser was used for liposomes, whereas a lime (561 nm, 50 mW) solid-state laser was used for light-activated liposomes, NLCs, and hexosomes. Movies were recorded at a 50 ms temporal resolution using SlideBook 6 software (Intelligent Imaging Innovations). Imaging was performed at 37 °C. The samples were kept at 37 °C for 20 min prior to visualization. Movements were tracked using Imaris 9.2 software (Bitplane AG, Zurich, Switzerland) and analyzed by @msdanalyzer (MATLAB plugin)[19] to extract the time-dependent mobility values derived from a large ensemble of particles (number of trajectories, $N \geq 50$). At least 3 independent experiments were performed for each particle type.

2.9. Calculation of the Diffusion Coefficient in Vitreous (D_v) and Theoretical Diffusivity in Water (D_w). The mean-squared displacement (MSD) of particle trajectories was computed with the mobility track analyzer (@msdanalyzer)[19] over the entire ensemble of particles. The diffusion coefficient in vitreous D_v was calculated from the slope of the linear part of the MSD vs time plot (eq 1):

$$D_v = \frac{\mathrm{MSD}_{(\tau)}}{2d\tau} \quad (1)$$

where d is the dimensionality of the track ($d = 2$ for a two-dimensional track), and τ is the time delay for the calculated displacement. The theoretical diffusivity in water D_w was calculated with the Stokes−Einstein equation (eq 2):

$$D_w = \frac{RT}{6\pi\eta r N_A} \quad (2)$$

where R is the gas constant (8.314 J K^{-1} mol^{-1}), T is the temperature (310.15 K), η is the viscosity of water at 37 °C (6.90×10^{-4} kg m^{-1} s^{-1}), r is the radius of the particle, and N_A is the Avogadro constant (6.022×10^{23} mol^{-1}). The particle radii were obtained from DLS measurements.

2.10. Porcine Vitreous Preparation for Proteomics. Pig eyes were obtained from a local slaughterhouse (HKScan Finland Oyj) and processed within 24 h of slaughter. The vitreous was excised and pooled during homogenization on an ice bath with 25 strokes using a glass tissue homogenizer. This was followed by centrifugation at 3200*g* for 1 h at 4 °C and filtration through Minisart hydrophilic regenerated cellulose syringe filters (0.45 and 0.22 μm, Sartorius, Göttingen, Germany) to remove cells and other debris. The pooled vitreous was stored at −80 °C until use, thawed in a 37 °C water bath, and vortexed before injection into the surface plasmon resonance instrument's flow cell.

2.11. Determination of Protein Corona Thickness and Protein Amount with Surface Plasmon Resonance. The measurements were conducted as described earlier with an MP-SPR Navi 220A (BioNavis Ltd., Ylöjärvi, Finland) using 670 and 785 nm incident lasers.[15] Anionic liposomes AL1-PEG and AL2 (50 nm, 500 μL, 16×10^{12} particles) were injected for 5 min until saturation of the custom sensor that can immobilize a maximum of 13.2×10^9 particles with 55 mm^2 active surface area.[20] Unbound liposomes were flushed off with buffer (HEPES 10 mM, NaCl 150 mM, pH 7.4), and the undiluted porcine vitreous was injected for ca. 5 min at a flow rate of 50 μL min^{-1} (association phase). The protein concentration by the BCA assay was 1.5 mg mL^{-1}, and the exposure was 0.25 mL with 375 μg of protein per replicate or 1.4 pg nm^{-2} min^{-1}. The soft corona protein fraction was

https://dx.doi.org/10.1021/acs.molpharmaceut.0c00411
Mol. Pharmaceutics 2021, 18, 699−713

flushed off with buffer, revealing the hard corona (HC; dissociation phase). After a buffer wash-out period, the hard corona protein fraction was eluted off the sensor together with the liposomes using Rapigest SF (0.1% w/v in mqH_2O, Waters Inc., Milford, MA, USA; Merck KGaA). These samples of the hard and soft corona were collected for proteomics studies into Protein LoBind tubes (Eppendorf AG) and stored at −20 °C. Flow-through vitreous on a saturated sensor was used as the source control. A dedicated sensor was used for each of the formulations, and the measurement was repeated 3−4 times on the same sensor, which was rejuvenated with CHAPS (20 mM, Sigma-Aldrich), ethanol (70%, Altia Oyj, Helsinki, Finland), mqH_2O (Merck KGaA), and stored at 4 °C immersed in CHAPS.

The SPR response based on the equation by Jung,[21] following the formalism of Rupert,[22] can be simplified to yield the thickness (eq 3):

$$R_n = S(dn/dC_*)_n c_n c_{*,n}(\pi d_n l_n)(1 - e^{-d_n/\delta}) \quad (3)$$

where n = nanoparticle. If p = protein and l = liposome, equal surface density of nanoparticles and approximation $d_l = d_p$ means that

$$c_l = c_p \qquad d_l = d_p$$

$$\rightarrow \frac{R_l}{(dn/dC_*)_l c_{*,l} l_l} = \frac{R_p}{S(dn/dC_*)_p c_p l_p}$$

$$\rightarrow \frac{R_p}{R_l} = \frac{(dn/dC_*)_p}{(dn/dC_*)_l}\frac{c_{*,p}}{c_{*,l}}\frac{l_p}{l_l}$$

$$\rightarrow l_p = \frac{R_p}{R_l}\frac{(dn/dC_*)_l}{(dn/dC_*)_p}\frac{c_{*,l}}{c_{*,p}} l_l$$

$$\approx \frac{R_p}{R_l}\frac{0.135}{0.182}\frac{1.05\ \mathrm{g/cm^3}}{c_{*,p}} \times 5\mathrm{nm} \approx \frac{3.894\ \mathrm{g/cm^3}}{c_{*,p}}\frac{R_p}{R_l} n \quad (4)$$

For the upper limit in eq 4, $c_{*,p}$ = 0.547 × 1.35 g/cm^3 = 0.738 g/cm^3 (surface coverage according to random sequential adsorption), and for the lower limit, $n = 1.40 \rightarrow c_{*,p}$ = 0.373 g/cm^3.[23] The protein amount (ng cm^{-2}) on the liposome that corresponds to the high and low estimates for HC and SC thickness was approximated using $\Gamma = d_p \times c_{*,p} \times 100$.

The SPR responses at the highest points of the association and the lowest of the dissociation phases were used for the soft and hard corona thickness calculations, respectively.

2.12. Proteomics Sample Preparation and Nanoliquid Chromatography−Tandem Mass Spectrometry. Sample preparation was conducted as previously, following the timed elution of the protein corona fractions using microfluidics.[15] The SPR-eluted samples were dried at 30 °C overnight using a Concentrator Plus (Eppendorf AG) in aqueous solution mode and stored until digestion as pellets at −20 °C. The pellets for the three to four independent biological replicates from AL1-PEG and AL2 were resuspended in ammonium bicarbonate buffer (AMBIC, 50 mM, pH 7.8). Prior to resuspension, the source vitreous was solubilized in RapiGest SF (0.2%, Waters Inc.). The protein concentration of each sample and the porcine vitreous source was determined with the BCA protein assay (Thermo Fisher Scientific, Waltham, MA, USA). Samples were either diluted further or pipetted directly to a final volume of 50 μL in AMBIC at a final protein amount of 7 μg. Tryptic peptides were prepared using the in-solution tryptic digestion and guanidination kit (Thermo Fisher Scientific) according to manufacturer's instructions but without guanidination. After digesting the samples overnight, formic acid was added to a concentration of 0.1%, followed by a 45 min incubation at 37 °C and 15 min centrifugation at 13 000 rpm to remove particulate debris and Rapigest SF. One sample of AL1-PEG HC was lost during sample preparation. Samples were loaded into an Easy-nLC 1200 (Thermo Fisher Scientific) in 250 μL autosampler microvials (Thermo Fisher Scientific). Chromatographic separation of peptides (100 ng) was carried out in commercially packed Acclaim PepMap C18 columns (2 mm, 100 Å, 75 mm, 15 cm, Thermo Fisher Scientific). Peptides were loaded in buffer A (5% acetonitrile and 0.1% formic acid) and eluted with a 3 h linear gradient from 5% to 30% buffer B (80% acetonitrile and 0.1% formic acid). Three biological replicates were sequentially injected with two 15 min wash runs and a 1 h blank run. Mass spectra were acquired using a Top N data-dependent method with an automatic switch between full MS and MS/MS (MS2) scans with an Orbitrap Fusion instrument (Thermo Fisher Scientific) using a 120 000 resolution, 350−1800 m/z mass range, and a 4e5 ion AGC target for the full MS scan, followed by a 30 000 resolution and 5e4 ion AGC target, with a 2 m/z isolation window and a 30 s dynamic exclusion for MS2 spectra acquisition. Column performance was monitored with intermittent injections of a BSA peptide mix (50 fmol, Bruker Corp., MA, USA) and tracking for carry-over peptides in the double-wash runs.

2.13. Proteomics Data Processing and Analysis. Protein groups identification and quantification were carried out with the MaxQuant v. 1.6.1.0,[24] with the UniProtKB FASTA file for *Sus scrofa* containing 40 701 protein and 23 223 gene entries, to which 245 commonly observed contaminants and all reverse sequences were added. Differential abundance analysis and hierarchical clustering were carried out with the Perseus data analysis software version 1.6.5.0.[25] Protein identifications with nonzero intensity values in at least three samples were retained for comparisons, and corresponding pI and gene name annotations were added. Abundance values were log2 transformed, protein identifications classified as only identified by site, and reverse sequences along with potential contaminants were filtered out from the main data frame. One AL1-PEG HC sample was deleted as an outlier before assigning groups for multiple sample testing. ANOVA multiple sample testing with a Benjamini-Hochberg FDR of 0.05 was performed on the assigned groups (source, hard corona, and soft corona), followed by specific two-sample Student's t tests with Benjamini-Hochberg FDR correction. The ExPASy ProtParam tool (https://web.expasy.org/protparam/) was used to compute the grand average of hydropathicity (GRAVY), as well as the theoretical pI and molecular weight for annotations not found in the database. To assess coverage versus reference proteomes, supplementary files with intensity data were obtained from vitreous proteome studies that have mapped the composition in healthy humans,[26−29] and other species,[30−32] converted to gene names using UniProtKB, the unmapped identifications were excluded, and the proteomes were compared against our protein identifications using a Venn diagram software (http://bioinformatics.psb.ugent.be/webtools/Venn/). Functional analysis was conducted on gene sets using GeneMANIA (http://genemania.org). Addi-

https://dx.doi.org/10.1021/acs.molpharmaceut.0c00411
Mol. Pharmaceutics 2021, 18, 699−713

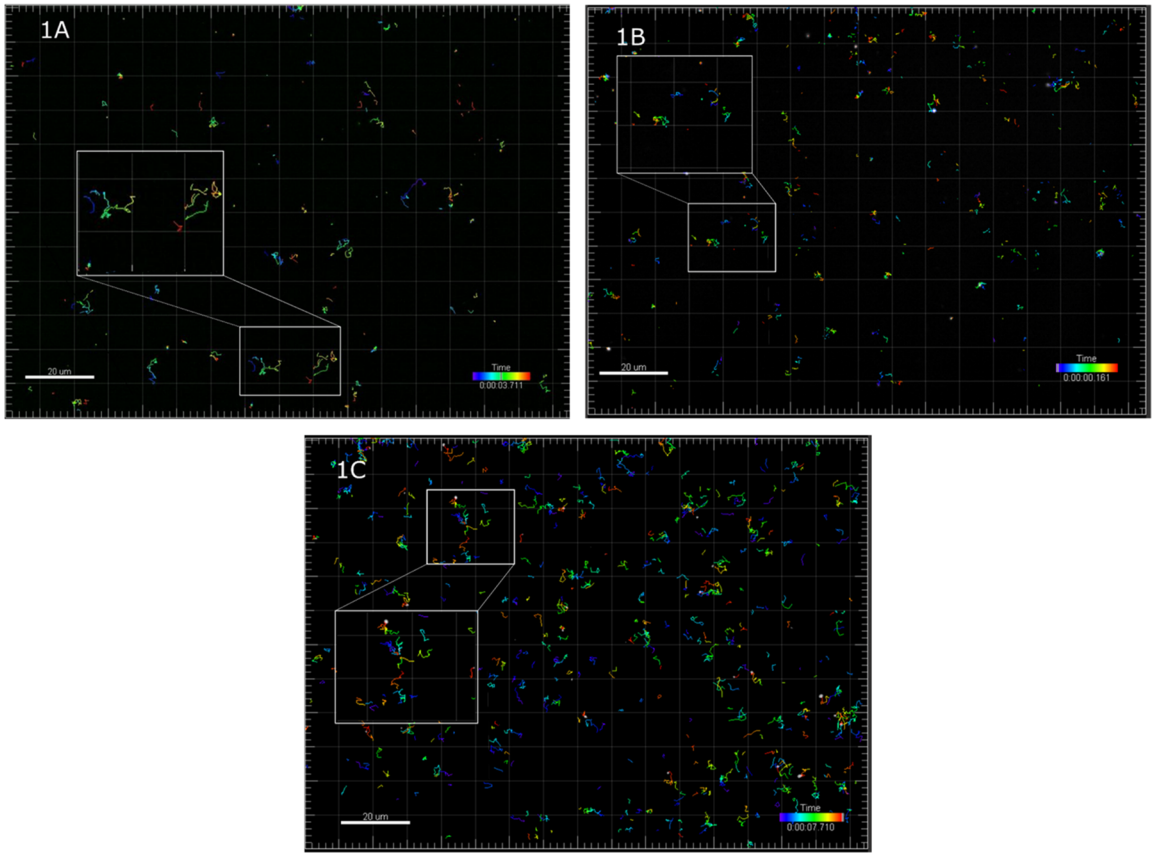

Figure 1. Trajectories of liposomal formulations in the intact porcine vitreous. Cationic PEGylated liposomes CL3-PEG (1A) are more mobile (D_v = 0.11 $\mu m^2 s^{-1}$) compared to the non-PEGylated formulation CL4 (1B) (D_v = 0.007 $\mu m^2 s^{-1}$). Anionic non-PEGylated light-activated liposomes AL6 (1C) have clearly more expanded trajectories (D_v = 0.7 $\mu m^2 s^{-1}$). The inserts show a magnified view of selected tracks.

tional data analysis and statistics were conducted with Prism 8.2.1 (GraphPad Software Inc., La Jolla, CA, USA).

3. RESULTS

3.1. Particle Size and ζ Potential. The lipid composition, the hydrodynamic diameter (size), the polydispersity index (PdI), and the ζ potential of all formulations are presented in Table 1. The PdI for most formulations was less than 0.4. Particle size and ζ potential measurements show that labeling did not affect the physicochemical properties of the formulations.

3.2. Vitreal Mobility of Light-Activated Liposomes. We prepared 36 different formulations of light-activated liposomes with negative, neutral, and positive charges. Each category was further divided depending on the liposome size (<50 nm, 100−200 nm, and >200 nm), PEGylation, and the presence of indocyanine green (ICG). Representative vitreal mobility tracks for positively charged non-PEGylated (D_v = 0.007 $\mu m^2 s^{-1}$) and PEGylated (D_v = 0.11 $\mu m^2 s^{-1}$) liposomes and for negatively charged non-PEGylated (D_v = 0.7 $\mu m^2 s^{-1}$) liposomes are presented in Figure 1. Within the same experiment, cationic liposomes display a bimodal behavior implying that a major fraction of the particles are immobile, while some trajectories span longer distances within the time scale of the measurement (Figure 1A,B). The heterogeneity in the diffusion of cationic liposomes was also reflected in the distribution of track length and speed of particles (e.g., CL1-PEG compared to CL2, Figure S1).

Anionic light-activated liposomes up to 300 nm in size had diffusion coefficients in vitreous that were 9−14 times slower than the calculated diffusion coefficients in water (Figure 2 and Table S1) indicating that the vitreous poses a minor barrier for these types of nanoparticles. Moreover, neither PEGylation nor the presence of ICG affected liposomal mobility. The diffusion of neutral light-activated liposomes decreased moderately with increasing liposome size. The mobility of small (<50 nm) and medium-sized (100−200 nm) PEGylated neutral light-activated liposomes is comparable to anionic liposomes (D_w/D_v = 11−13), whereas larger and non-PEGylated light-activated liposomes encounter a higher resistance from the vitreous barrier (D_w/D_v = 16−29) (Figure 2). PEG improves the diffusion of liposomes, even though the effect is still moderate. Apparently, ICG does not affect neutral liposome mobility. Based on the results of cationic light-activated liposomes, PEGylation dramatically increases their mobility, despite the fact that the liposomes still had a positive charge. The D_w/D_v ratios of PEGylated cationic light-activated liposomes are 1 order of magnitude smaller compared to their non-PEGylated counterparts: D_w/D_v (PEG) = 126−170, D_w/D_v (without PEG) = 1770−3486 (Figure 2). In addition, size increase has an insignificant effect on their mobility: for small PEGylated liposomes (<50 nm) D_w/D_v = 126, whereas for large PEGylated liposomes (>200 nm) D_w/D_v = 170 (Figure 2). Again, ICG does not affect the mobility of cationic liposomes (Supporting Information).

3.3. Vitreal Mobility of Rigid-Membrane Liposomes. Rigid-membrane liposomes followed a similar pattern as the

https://dx.doi.org/10.1021/acs.molpharmaceut.0c00411
Mol. Pharmaceutics 2021, 18, 699−713

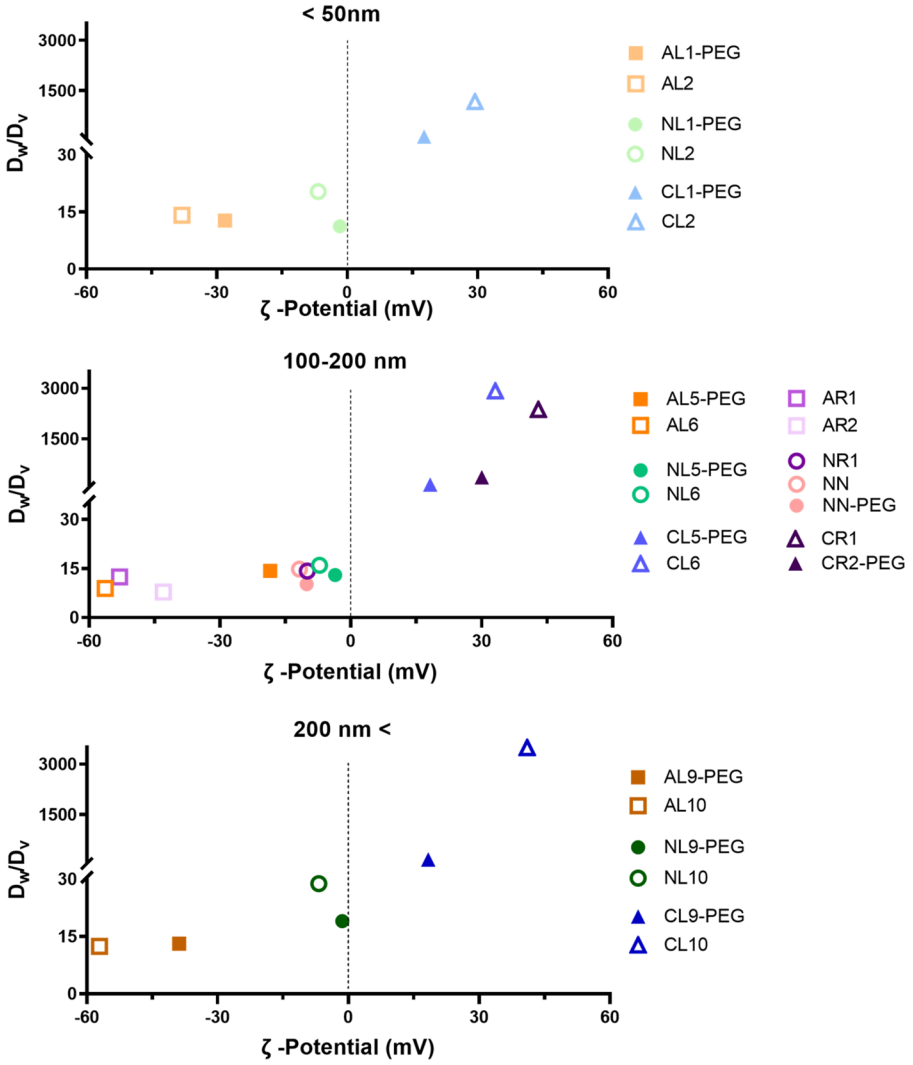

Figure 2. Effect of surface charge, particle size, and surface modification (PEG and ICG) on the mobility of lipid-based formulations in the vitreous based on the corresponding D_w/D_v ratios. Formulations are categorized in three graphs based on their size range: <50nm (top), 100−200 nm (middle), and >200 nm (bottom). PEGylated formulations are displayed in filled symbols, and the empty symbols represent the non-PEGylated formulations. (A) anionic, (N) neutral, (C) cationic formulation; (L) light-activated liposomes and controls; (R) rigid-membrane liposomes; (N) nanostructured lipid carriers (NLCs). See Table 1 for the detailed lipid compositions. D_v was derived from the ensemble-averaged MSD at a time scale of 1 s from at least 50 trajectories in 3 different experiments. Values for D_v (including the standard deviation), D_w, and D_w/D_v ratios are provided as Supporting Information. The D_w/D_v ratio for hexosomes is 8.7; the data is not presented in this figure due to the missing ζ potential value.

light-activated liposomes (Figure 2). The anionic formulations AR1 and AR2 and the similarly sized neutral formulation NR1 diffuse rapidly in the vitreous (D_w/D_v = 8−14), whereas the cationic liposome CR1 was practically immobile (D_w/D_v = 2370). As with light-activated liposomes, PEGylation of the cationic rigid-membrane liposomes (CR3-PEG) increased liposomal diffusion by 1 order of magnitude (D_w/D_v = 351).

3.4. Vitreal Mobility of Hexosomes and Nanostructured Lipid Carriers (NLC). In addition to the liposomal formulations, other lipid-based formulations were tested to evaluate the robustness of the results. Although hexosomes were larger than liposomes at 300 nm, their D_w/D_v = 9 fell within the same range measured for the liposomal formulations with a neutral charge (Figure 2). NLCs with and without PEGylation followed the same trend, with D_w/D_v = 15 and 10, respectively (Figure 2).

3.5. Vitreal Corona Thickness of Anionic Light-Activated Liposomes. The anionic light-activated liposomes AL1-PEG and AL2 were chosen for analysis of their soft (SC) and hard (HC) protein coronae, since they showed high mobility in the vitreous regardless of the lack or presence of PEGylation (4 mol%). The SC was 3.1 ± 1.1 nm for AL1-PEG and 2.5 ± 0.9 nm for AL2, whereas the HC was approximately 2.2 ± 0.9 nm for both formulations (Figure 3). There were no significant differences in protein corona thickness between AL1-PEG and AL2. The SC and HC protein amounts were 145 ± 28 ng cm^{-2} and 120 ± 29 ng cm^{-2} and 110 ± 23 ng cm^{-2} and 111 ± 21 ng cm^{-2} for AL1-PEG and AL2, respectively (Figure 3).

3.6. Vitreal Corona Protein Composition of Anionic Light-Activated Liposomes. In total, 535 nonredundant proteins were identified in the source porcine vitreous and at least one sample of the corona subsections by nLC-ESI-MS/MS (Supporting Information File 1). These included 101 proteins that have not been previously reported in proteomic studies of the human vitreous[26−29] and 88 previously unknown

https://dx.doi.org/10.1021/acs.molpharmaceut.0c00411
Mol. Pharmaceutics 2021, 18, 699−713

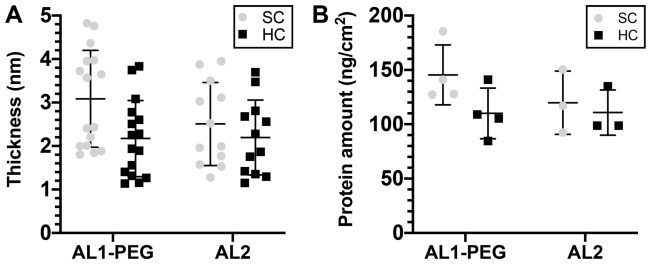

Figure 3. Surface plasmon resonance analysis of soft (SC) and hard (HC) corona formation on sensor-immobilized anionic liposomes with (AL1-PEG, 50 nm) and without (AL2, 50 nm) polyethylene glycol from replicate measurements with (A) thickness and (B) corresponding protein amount. Individual data points are displayed with mean and standard deviation.

proteins when dog, rabbit, and mouse vitreal proteomes were also included (Figures S2 and S4).[30−32] 504 proteins found in at least three samples were retained for analysis (Supporting Information File 2 and 3), which resulted in 76 differentially abundant proteins (Figure 4). While there is a clear difference between the groups for HC, SC, and vitreous, the compositions within the HC and SC subsections are similar. None of the SC enriched proteins were detected in any of the HC replicates. Functional analysis revealed that three HC and two SC proteins are GAPDH physical interaction partners (Figure S5). The significantly enriched proteins are listed in Table 2, and the details are provided in the Supporting Information. There were no statistically significant differences in preferential enrichment between two anionic liposome formulations for HC, and only vesicle-fusing ATPase (NSF) enrichment was significantly less depleted in the SC of AL2 ($p < 0.05$). The liposome corona enriched proteins included 45 proteins reported in silica and gold nanoparticle coronae (Table S5).[30] Venn diagrams that show all of the overlapping and distinctive proteins, as well those with ANOVA-significant differences between the hard and soft coronas per formulation, along with lists of all and significantly different protein-encoding genes per sample, are provided as Supporting Information (Figures S6 and S7, Tables S6 and S7, Tables S8 and S9).

4. DISCUSSION

The vitreous humor is the first physiological environment encountered by intravitreally injected nanoparticles. Upon intravitreal injection, the synthetic identity of nanoparticles evolves into a biological identity[34] that shapes the pharmacokinetic behavior and pharmacodynamic response,

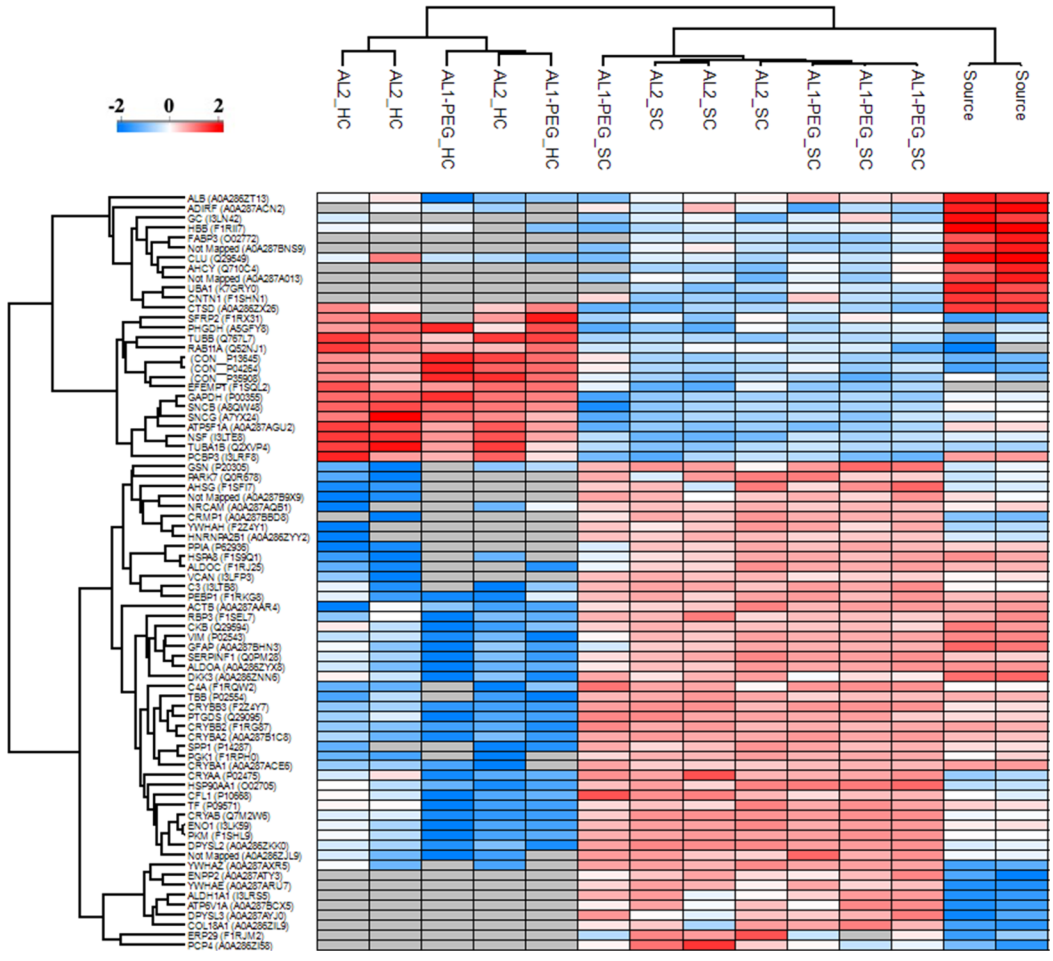

Figure 4. Heatmap of Z-score normalized hierarchical cluster analysis with 76 differentially abundant proteins that distinguish between the hard (HC) and soft corona (SC) subsections and the porcine vitreous (source). The range is two standard deviations from the mean in both directions for relative enrichment (red) and depletion (blue) on a log2 scale. The gray color indicates that the protein was not identified in the sample replicate.

https://dx.doi.org/10.1021/acs.molpharmaceut.0c00411
Mol. Pharmaceutics 2021, 18, 699−713

Table 2. Relative Protein Enrichment in the Hard Corona (HC) and Soft Corona (SC) of Anionic Light-Activated Liposomes (AL1-PEG and AL2, 50 nm) and Porcine Vitreous Sources Based on the ANOVA Hierarchical Clustering Analysis[a]

protein	gene	name	MW [kDa]	pI[b]	GRAVY[c]	preference[d]
		Hard Corona (HC)				
F1RX31	SFRP2	secreted frizzled-related protein 2●	33.3	7.19 (−)	−0.277	AL2 (1.02:0.90)
A5GFY8	PHGDH	D-3-phosphoglycerate dehydrogenase	56.8	6.54 (−)	0.102	AL1-PEG (1.54:0.75)
Q767L7	TUBB	tubulin β chain	49.7	4.65 (−)	−0,348	AL2 (1.35:0.96)
Q52NJ1	RAB11A	Ras-related protein Rab-11A	24.4	6.26 (−)	−0.421	AL2 (1.04:0.90)
CON__P13645	KRT10	keratin, type I cytoskeletal 10[f,g]	58.8	5.13 (−)	−0.624	AL1-PEG (1.43:1.02)
CON__P04264	KRT1	keratin, type II cytoskeletal 1[f,g]	66.0	8.15 (+)	−0.626	AL1-PEG (1.45:0.97)
CON__P35908	KRT2	keratin, type II cytoskeletal 2 epidermal[f,g]	65.4	8.07 (+)	−0.471	AL1-PEG (1.42:1.01)
F1SQL2	EFEMP1	EGF-containing fibulin-like extracellular matrix protein 1●	54.9	4.77 (−)	−0.313	AL2 (1.10:0.98)
P00355	GAPDH	glyceraldehyde-3-phosphate dehydrogenase	35.8	8.30 (+)	−0.069	AL1-PEG (1.32:1.16)
A8QW48	SNCB	β-synuclein	14.1	4.32 (−)	−0.491	AL2 (1.24:1.05)
A7YX24	SNCG	γ-synuclein●●	13.0	4.78 (−)	−0.368	AL2 (1.37:0.85)
A0A287AGU2	ATP5F1A	ATP synthase subunit α[g],●●	59.4	8.95 (+)	−0.073	AL2 (1.39:0.73)[I]
I3LTE8	NSF	vesicle-fusing ATPase	84.3	7.23 (−)	−0.280	AL2 (1.49:0.78) **[I]
Q2XVP4	TUBA1B	tubulin α-1B chain●	50.2	4.82 (−)	−0.230	AL2 (1.64:0.53)
I3LRF8	PCBP3	poly(rC)-binding protein 3	28.2	8.34 (+)	−0.046	AL2 (1.26:0.45)
		averages[e]	42.0	6.34	−0.235	protein d: 4.6 nm
		Soft Corona (SC)				
A0A287AXR5	YWHAZ	14−3−3 protein ζ/δ[g]	26.7	4.93 (−)	−0.494	AL2 (0.77:0.74)
A0A287ATY3	ENPP2	ectonucleotide pyrophosphatase/phosphodiesterase family member 2[g],●	105.1	8.46 (+)	−0.582	AL2 (0.51:0.46)
A0A287ARU7	YWHAE	14−3−3 protein ε[g]	27.4	4.77 (−)	−0.440	AL2 (0.51:0.49)
I3LRS5	ALDH1A1	retinal dehydrogenase 1●	22.9	6.44 (−)	−0.085	AL1-PEG (0.65:0.23)
A0A287BCX5	ATP6V1A	V-type proton ATPase catalytic subunit A[g]	64.2	5.38 (−)	−0.165	AL1-PEG (0.51:0.41)
A0A287AYJ0	DPYSL3	dihydropyrimidinase-related protein 3[g]	57.8	5.85 (−)	−0.244	AL1-PEG (0.73:0.11)
A0A286ZIL9	COL18A1	collagen α-1(XVIII) chain[g]	129.9	5.65 (−)	−0.618	AL1-PEG (0.63:0.19)
F1RJM2	ERP29	endoplasmic reticulum resident protein 29	29.3	7.14 (−)	−0.295	AL2 (1.05:−0.20) **[I]
A0A286ZI58	PCP4	calmodulin regulator protein PCP4	6.8	6.21 (−)	−1.332	AL2 (1.04:−0.11)
		averages[e]	52.2	6.09	−0.473	protein d: 5.0 nm
		Vitreous Source				
A0A286ZT13	ALB	serum albumin[g],●	68.2	5.99 (−)	−0.425	AL2: HC, AL1-PEG: SC
A0A287ACN2	ADIRF	adipogenesis regulatory factor[g],●●	7.8	5.21 (−)	−0.491	AL2: HC, SC
I3LN42	GC	vitamin D-binding protein●	53.5	5.41 (−)	−0.433	AL1-PEG: SC
F1RII7	HBB	hemoglobin subunit β●	16.2	6.93 (−)	−0.053	AL1-PEG: HC, SC
O02772	FABP3	fatty acid-binding protein, heart	14.7	6.26 (−)	−0.209	AL2: SC
A0A287BNS9	unmapped	ubiquitin-like domain-containing protein[g]	15.2	9.96 (+)	−0.509	AL2: SC
Q29549 (*Bos taurus*) (CON__P17697)	CLU	clusterin●	51.8	5.61 (−)	−0.614	AL2: HC, AL1-PEG: SC

https://dx.doi.org/10.1021/acs.molpharmaceut.0c00411
Mol. Pharmaceutics 2021, 18, 699−713

Table 2. continued

protein	gene	name	MW [kDa]	pI[b]	GRAVY[c]	preference[d]
		Vitreous Source				
Q710C4	AHCY	adenosylhomocysteinase	47.7	5.99 (−)	−0.088	AL2: SC
A0A287A013	unmapped	Ig-like domain-containing protein[g]	12.4	5.51 (−)	−0.875	AL1-PEG: SC
K7GRY0	UBA1	ubiquitin-like modifier-activating enzyme 1 isoform X2	107.5	5.34 (−)	−0.262	AL2: SC
F1SHN1	CNTN1	contactin-1	113.6	6.05 (−)	−0.338	AL1-PEG: SC
A0A286ZX26	CTSD	cathepsin D[g]	44.1	8.01 (+)	0.055	AL2: HC, AL1-PEG: SC
		averages[e]	46.1	6.36	−0.354	protein *d*: 4.8 nm

[a]Proteins are listed in the order displayed in the heatmap with their isoelectric point (pI), molecular weight (MW), and grand average of hydropathicity (GRAVY) along with averages. The liposome with higher relative enrichment with the corresponding log2-fold change for both formulations and the calculated average effective protein diameter thickness in the HC, SC, or vitreous source groups are also provided. Statistically significant differences in protein enrichment between the liposome formulations within HC and SC are indicated by **. The proteins previously reported in gold and silica nanoparticle coronae and the proteins that have not been previously identified in the human vitreous are marked by • and ••, respectively. [b]pI with a predominant charge in the vitreous at neutral pH 7.4. [c]Grand average of hydropathicity (GRAVY) calculated with sequence pI using the ExPASy ProtParam tool. It is the sum of amino acid hydropathicity values divided by the length of the protein, whereby hydrophobicity increases with increasing positive score.[33] [d]Preference toward formulation based on relative enrichment (comparison of replicate average log2-fold changes). Statistically significant differences between formulations within the groups HC and SC based on multiple *t* tests with Benjamini-Hochberg FDR correction are indicated by ** ($p < 0.005$ and $q < 0.05$). [e]Column averages and the calculated average effective protein diameter based on the MW (tight-packed monolayer thickness). [f]Contaminants excluded from the column averages and associated analysis. [g]Theoretical pI and MW calculated with the ExPASy ProtParam tool. [h]Reported on gold and silica nanoparticles by Jo.[30] [I]Not previously reported in human vitreous by Semba,[26] Aretz,[27] Yee,[28] and Skeie.[29]

possibly via altered intracellular delivery properties. It is thus meaningful to characterize nanoparticles both in their original formulation and also in the physiologic environment of the vitreous humor. Here, we evaluate the diffusion of lipid-based formulations in vitreous compared to water and carry out a comprehensive description of the vitreal protein corona of the formulations with the most promising attributes for ocular drug delivery. Understanding the biological identity of intravitreally administered nanoparticles will greatly benefit the development of novel nanoparticle-based ocular treatments.

4.1. Vitreal Mobility Depends on Lipid-Based Formulation Charges. After intravitreal administration, nanoparticles must be able to overcome the vitreous barrier to reach their target tissue (e.g., the retina), where they are eventually internalized by cells. Here their cargo (such as small regulatory RNAs, proteins, and peptides) must be released to produce a therapeutic effect. Since the blood−ocular barriers preclude the posterior elimination route, nanoparticles are believed to be eliminated from the eye via the slower anterior elimination route, which goes through the posterior chamber and anterior chamber and via the trabecular meshwork to the canal of Schlemm. In order to gain access to the posterior chamber, nanoparticles must diffuse through the vitreous humor. Our work shows that the vitreous is a weak barrier for the diffusion of negatively charged and neutral lipid-based formulations; however, given its anionic properties, the vitreous severely restricts the diffusion of cationic formulations. Formulation charge is thus the most important factor regulating the mobility of lipid-based nanoparticles in the vitreous humor. Our results are in line with earlier studies also performed in intact vitreous, which, however, evaluated a much narrower selection of particles and did not include liposomes.[6,7] In addition, our work determines that PEGylation rescues the mobility of cationic liposomes without affecting their overall charge, clearly indicating the steric shielding effect of PEG coating on particle diffusion. Compared to previous work, we found the D_w/D_v ratio of anionic lipid-based nanoparticles in porcine vitreous ($D_w/D_v = 6-14$) to be slightly higher than the ratio of anionic polystyrene nanoparticles of the same size in bovine vitreous ($D_w/D_v = 2-3$)[6]. This may be due to differences in composition between porcine and bovine vitreous humor, but also to the different chemical composition of the nanoparticles (lipid-based formulations vs polystyrene). Käsdorf found the mobile fractions of anionic DOPG/DOPE liposomes (185 nm, −50.2 mV) also to be slightly lower in porcine compared to bovine vitreous.[3] As others have already pointed out,[6,7] we have also observed mobility differences within the same particle population (see Figure 1A,B). For example, while the majority of cationic light-activated liposomes showed restricted mobility, some particles had longer trajectories. This phenomenon may be explained by the heterogeneous distribution of macromolecules (collagens and glycosaminoglycans) throughout the vitreous.[2] Thus, the microenvironment for individual liposomes may be different, and this will affect their mobility.

4.2. Protein Corona Formation on Anionic Light-Activated Liposomes. Protein binding may be another important factor that significantly alters the vitreal pharmacokinetics of nanoparticles. Our analysis of the overlap in protein identifications between our study and previous reports was 81.1% with human and 83.6% with human, dog, rabbit, and mouse. The measured protein concentration and composition of porcine vitreous, therefore, replicate the situation in the healthy human eye, although there is wide variation in the literature values (0.2−4.7 mg).[35−39] Its viscoelastic properties and structure are also very similar.[40] PEGylation does not significantly influence corona thickness in porcine vitreous, since the HC was 2.2 nm and the SC was 2.5−3.1 nm for both formulations. Earlier, we observed that PEGylation did not influence the HC thickness on similar light-activated liposomes in undiluted human plasma.[15] Since the calculated effective

https://dx.doi.org/10.1021/acs.molpharmaceut.0c00411
Mol. Pharmaceutics 2021, 18, 699−713

protein diameter is approximately 4.6 nm for the HC and 5.0 nm for the SC, assuming tight packing, we can deduce that the vitreal protein corona is sparse and only contributes to a 10−12% increase in diameter. Recent studies on PEGylated liposomes in serum and plasma have also demonstrated that the HC was sparse, and surface protein coverage is low,[41−43] which is consistent with our findings.

The predominant charge of most of the adsorbed proteins is negative, suggesting that anionic liposomes retain their negative surface charge in the neutral ocular environment and in ex vivo vitreous with pH 8.[44,45] Most of the significantly enriched proteins in the corona and vitreous were hydrophilic, with the exception of D-3-phosphoglycerate dehydrogenase (PHGDH). Functional analysis showed that a large number of HC enriched proteins were physical protein−protein interaction partners of glyceraldehyde-3-phosphate dehydrogenase (GAPDH), and the keratin contaminants may have contributed to the enrichment of some SC proteins (Supporting Information). In addition to electrostatic and hydrophobic interactions, protein−protein interactions related to the proteins' biological functions may, therefore, also contribute to their enrichment in the corona.

While there are no previous reports on vitreal corona formation on liposomes, Jo[30] studied HC formation on anionic 20 and 100 nm gold and silica nanoparticles in dilute dog vitreous. They reported an increase in hydrodynamic diameter corresponding to 5−8 nm HC thickness, about 2-fold compared to our measurement. They found a weak positive correlation with pI and GRAVY values, and a significant number of proteins had a pI > 7.4, noting that protein adsorption is driven by electrostatic and hydrophobic properties of the proteins, irrespective of the core material. There was no evident correlation between charge, hydropathicity, and protein preference for the liposomes AL1-PEG or AL2, and attractive electrostatic forces were not dominant, since anionic liposomes were found to bind predominantly negatively charged proteins, which might be explained by Stern layer formation.[46] Regardless of the different incubation conditions, there was a 75% overlap overall in protein identifications on gold, silica, and liposome coronae. Together these observations suggest that protein-specific rather than particle-specific factors are drivers of protein adsorption on nanoparticles in the vitreous, as originally observed by Jo.[30]

Since the corona thickness and protein composition of AL1-PEG (4 mol% PEG-2000) were not significantly different, it is possible that the traditional stealth properties of PEG are not directly applicable to the ocular environment. When the same anionic liposome formulations (100 nm) were subjected to undiluted plasma under the same experimental conditions, PEGylation had a clear effect on both HC and SC thickness and composition.[15] Nevertheless, the protein corona might influence biological interactions and affect the clearance and cell uptake of the liposomes. For instance, the enriched complement, 70 kDa and 90 kDa heat shock proteins may enhance particle removal by hyalocytes, retinal pigment epithelial cells, or ocular macrophages.[47−50] Recent studies in mice have shown that for intravenously injected nanoparticles, the combination of proteins in the corona, rather than a specific protein in the corona, influences biodistribution and cell uptake by liver and spleen.[10] This is probably the case also in the ocular environment and, therefore, the biological implications of corona formation should be addressed in future studies.

Our findings on similar compositions and thicknesses for both AL1-PEG and AL2 are consistent with their very similar diffusion behavior in the vitreous. This is not surprising, since the particle sizes after protein corona formation are still only one-tenth of the vitreous mesh size, and the surface charge is expected to remain negative. Based on our results, protein corona formation does not influence the mobility of anionic nanoparticles in the vitreous, and the benefit of PEG as a stealth approach was not evident. On the other hand, the protein corona may have an impact on the cellular removal mechanisms or on the uptake and intracellular distribution in the target cells.

4.3. Convection, Not Diffusion, Rules the Ocular Pharmacokinetics of Nanoparticles. Let us assume that diffusion is the only driving force affecting the mobility of nanoparticles in the vitreous humor; then using eq 1, we can calculate the time t required by a nanoparticle to move for a certain distance x in three dimensions:

$$t = \frac{x^2}{6D_v}$$

Table 3 summarizes the average time t required for an anionic lipid-based nanoparticle (100−200 nm, D_v = 0.5 $\mu m^2\ s^{-1}$) and for the IgG antibody bevacizumab (150 kDa), commonly used in the treatment of ocular diseases (D_v = 50 $\mu m^2\ s^{-1}$),[51] to travel the distance from the center of the vitreous gel to the retina (the vitreous radius), in human and in animal models commonly used in ocular pharmacokinetics and pharmacodynamics studies. In addition, the time required in liquefied vitreous ($D_{v,liq}$ = 5 $\mu m^2\ s^{-1}$ for a nanoparticle of 100 nm diameter and $D_{v,liq}$ = 72 $\mu m^2\ s^{-1}$ for an antibody of 4.5 nm radius are calculated with eq 2) is also shown.

Table 3. Average Travel Time (t) Needed to Reach the Retina for a Nanoparticle (Abbreviated as nano) and an Antibody (Abbreviated as ab) in Normal and Liquefied (liq) Vitreous, Assuming Exclusively Diffusion-Driven Distribution

	x [cm]	t_{nano}	t_{ab}	$t_{nano,liq}$	$t_{ab,liq}$
human	1[a]	1.1 years	3.9 days	39 days	2.7 days
rabbit	0.7[a]	0.5 years	1.9 days		
rat	0.2[a]	15.4 days	3.7 h		
mouse	0.04[b]	14.8 h	8.9 min		

[a]Vitreous radii from Hutton-Smith.[52] [b]Vitreous radius from Zhou.[53]

The role of diffusion in vitreal mobility is clearly different depending on the type of therapeutic (nanoparticle vs antibody) and on the size of the eyes. For a macromolecule, such as bevacizumab, vitreal diffusion plays an important role in both the ocular distribution and elimination. Indeed, the elimination half-life of bevacizumab was reported to be 7−10 days in humans,[54,55] 4−6 days in rabbits,[56,57] and 8 h in rats.[52] In the case of a nanoparticle, however, the results indicate that, especially in larger eyes (rabbits, humans), the vitreal diffusion is much too slow to have any effect on its pharmacokinetics. Barza,[58] for example, determined that the vitreal half-life of 60 nm and 400−600 nm liposomes in normal rabbit eyes ranged from 9 to 20 days, respectively. In other words, were the distribution and elimination of nanoparticles based solely on diffusion, then they would be retained in the vitreous of larger eyes for a much longer time. In addition, the time a

https://dx.doi.org/10.1021/acs.molpharmaceut.0c00411
Mol. Pharmaceutics 2021, 18, 699−713

Table 4. Péclet Numbers for a Nanoparticle and an Antibody in Normal and Liquefied Vitreous[a]

	Pe_{nano}	transport driven by	Pe_{ab}	transport driven by	$Pe_{nano,liq}$	transport driven by	$Pe_{ab,liq}$	transport driven by
human	66.7	convection	0.7	diffusion	6.7	convection	0.5	diffusion
rabbit	46.7	convection	0.5	diffusion				
rat	13.3	convection	0.1	diffusion				
mouse	2.7	convection and diffusion	0.03	diffusion				

[a]The Péclet number (Pe) indicates the ratio of the contributions to mass transport by convection and by diffusion. For all species, the velocity of the convective fluid flow in the rabbit vitreous, as estimated by Araie and Maurice,[59] was used.

nanoparticle requires to diffuse from the central vitreous to the retina is remarkably different in rodents (mice, rats) and in larger animals (rabbits, humans).

We can provide a simple estimate of the magnitude of the effect of diffusion and convection by means of a dimensionless number called the Péclet number (Pe) (eq 5), which is the ratio of the contributions to mass transport by convection to those by diffusion:

$$\mathrm{Pe} = \frac{\text{convection}}{\text{diffusion}} = \frac{VL}{D_v} \tag{5}$$

where V is the velocity of the convective fluid flow in the vitreous (2×10^{-5} cm min^{-1} in rabbit, as estimated by Araie and Maurice[59]), L is a characteristic length scale (in this case the vitreous radius), and D_v is the diffusion coefficient in vitreous. When Pe < 1 diffusion dominates, when Pe > 1 convection dominates, and when Pe ∼ 1, their influence is similar. The calculated Péclet numbers for a nanoparticle and for an antibody are shown in Table 4. Note that we had to use the velocity of the convective fluid flow in rabbits, since the values for other species, including humans, are not known. In larger eyes, the transport of nanoparticles takes place exclusively by convection; the mobility of antibodies, instead, is mostly governed by diffusion. For antibodies, the role of diffusion is more significant in smaller eyes.

Another important factor that may affect the ocular pharmacokinetics of intravitreally injected nanoparticles is the state of the vitreous humor, including changes in vitreous viscosity and composition. Ocular disorders that will benefit from the development of a nanoparticle-based drug delivery overwhelmingly affect elderly people. With aging, the vitreous humor undergoes progressive liquefaction (synchysis) and aggregation of collagen fibrils (syneresis), so that by the age of 80−90 years, more than half of the gel phase has turned into a liquid phase.[60] In this case, we can assume that the diffusion of intravitreally injected nanoparticles will be closer to the calculated diffusion coefficient in water. Coming back to the hypothetical exercise presented in Table 3, we can, therefore, assume $D_{v,liq} = 5\ \mu m^2\ s^{-1}$. Even such a minor increase in the mobility of a nanoparticle will significantly decrease the time required to reach the retina from 1.1 years to 39 days (Table 3). For an antibody, instead, liquefied vitreous only moderately affects its mobility, which decreases from 3.9 days to 2.7 days. The Péclet number for the nanoparticle in liquefied vitreous is 1 order of magnitude smaller compared to young vitreous (Table 4), assuming that the velocity of the convective fluid flow in liquefied vitreous remains the same. In the case of the antibody, on the contrary, the Péclet number is hardly affected by vitreous liquefaction, and diffusion remains the driving force. Thus, compared to young eyes, in aging eyes that have undergone liquefaction, diffusion may play a more important role in determining the ocular pharmacokinetics of nanoparticles, whereas the mobility of antibodies remains unaffected.

Regarding the composition of the vitreous humor, we must take into consideration patients who have undergone vitrectomy. Vitrectomy is a common surgical procedure that removes the vitreous humor and replaces it with an expansile gas or a liquid (perfluorocarbon liquids, semifluorinated alkanes, silicone oils, polymeric hydrogels).[37] The effect of these vitreous substitutes on the ocular pharmacokinetics of intravitreally injected nanoparticles is not known. In the case of macromolecules, however, published reports indicate no effect or slightly shorter half-lives for bevacizumab, ranibizumab, and aflibercept in vitrectomized eyes of rabbits and monkeys.[61−63] It is difficult to predict the behavior of nanoparticles in vitreous substitutes; nevertheless, if the velocity of the convective fluid flow remains constant, then it is likely that convection will still play an important role. If, however, the velocity decreases, then diffusion may gain influence. In addition, the pharmacokinetics of nanoparticles in vitrectomized eyes may also be influenced by other factors such as their stability and possible aggregation in vitreous substitutes.

5. CONCLUSION

Favorable vitreal pharmacokinetic properties are essential for the success of an intravitreal therapy based on nanoparticles. Our mobility study broadens prior work[5−7] by evaluating the vitreal diffusion of a wide selection of lipid-based formulations. Interestingly, our findings are pointing toward a convection-driven, rather than a diffusion-driven, distribution of nanoparticles in the vitreous humor. In addition, given the dramatic differences observed between rodent and rabbit/human eyes, we urge to carefully consider how the size of the eye affects nanoparticle distribution and likely complicates interspecies translation. Our study also provides insight into the previously unexplored formation of the protein corona on intravitreally injected liposomes. Further work is needed to elucidate the influence of the protein corona on the ocular biodistribution of liposomes, including their uptake by retinal cells.

■ ASSOCIATED CONTENT

Supporting Information

The Supporting Information is available free of charge at https://pubs.acs.org/doi/10.1021/acs.molpharmaceut.0c00411.

Descriptions, effect of charge, particle size, and surface modification, trajectories lengths and ensemble-averaged speeds, vitreal corona protein composition of anionic light-activated liposomes, diagram of nonredundant protein identifications, gene names and associated proteins, functional analyses, common gene sets, comparison of liposome corona, and protein-encoding genes (PDF)

Video S1 (MP4)

https://dx.doi.org/10.1021/acs.molpharmaceut.0c00411
Mol. Pharmaceutics 2021, 18, 699−713

Video S2 (MP4)
Video S3 (MP4)
Video S4 (MP4)
Video S5 (MP4)
Video S6 (MP4)
File 1: Protein name found the min 1 sample (XLSX)
File 2: Matrix filtered found in min 3 samples raw intensities sample averages (XLSX)
File 3: Significant ANOVA (XLSX)
File 4: ANOVA and *t* tests for selected contrast relative abundance sample averages (XLSX)

AUTHOR INFORMATION

Corresponding Author

Astrid Subrizi − *School of Pharmacy, Faculty of Health Sciences, University of Eastern Finland, 70210 Kuopio, Finland;* orcid.org/0000-0003-2170-4333; Phone: +358-40-0163407; Email: astrid.subrizi@uef.fi

Authors

Shirin Tavakoli − *Drug Research Program, Division of Pharmaceutical Biosciences, Faculty of Pharmacy, University of Helsinki, 00014 Helsinki, Finland*

Otto Kalevi Kari − *Drug Research Program, Division of Pharmaceutical Biosciences, Faculty of Pharmacy, University of Helsinki, 00014 Helsinki, Finland;* orcid.org/0000-0002-1201-5010

Tiina Turunen − *Drug Research Program, Division of Pharmaceutical Biosciences, Faculty of Pharmacy, University of Helsinki, 00014 Helsinki, Finland*

Tatu Lajunen − *Drug Research Program, Division of Pharmaceutical Biosciences, Faculty of Pharmacy, University of Helsinki, 00014 Helsinki, Finland*

Mechthild Schmitt − *Drug Research Program, Division of Pharmaceutical Biosciences, Faculty of Pharmacy, University of Helsinki, 00014 Helsinki, Finland*

Julia Lehtinen − *Drug Research Program, Division of Pharmaceutical Biosciences, Faculty of Pharmacy, University of Helsinki, 00014 Helsinki, Finland*

Fumitaka Tasaka − *Pharmaceutics & Pharmacology Department, Global R&D, Santen Pharmaceutical Co., Ltd., Ikoma, Nara 630-0101, Japan*

Petteri Parkkila − *Drug Research Program, Division of Pharmaceutical Biosciences, Faculty of Pharmacy, University of Helsinki, 00014 Helsinki, Finland;* orcid.org/0000-0002-2717-0232

Joseph Ndika − *Human Microbiome Research, Faculty of Medicine, University of Helsinki, 00290 Helsinki, Finland;* orcid.org/0000-0003-0669-1300

Tapani Viitala − *Division of Pharmaceutical Chemistry and Technology, Faculty of Pharmacy, University of Helsinki, 00014 Helsinki, Finland;* orcid.org/0000-0001-9074-9450

Harri Alenius − *Human Microbiome Research, Faculty of Medicine, University of Helsinki, 00290 Helsinki, Finland; Institute of Environmental Medicine, Karolinska Institutet, 171 77 Stockholm, Sweden;* orcid.org/0000-0003-0106-8923

Arto Urtti − *Drug Research Program, Division of Pharmaceutical Biosciences, Faculty of Pharmacy, University of Helsinki, 00014 Helsinki, Finland; Institute of Chemistry, St. Petersburg State University, 198504 St. Petersburg, Russia; School of Pharmacy, Faculty of Health Sciences, University of Eastern Finland, 70210 Kuopio, Finland;* orcid.org/0000-0001-6064-3102

Complete contact information is available at: https://pubs.acs.org/10.1021/acs.molpharmaceut.0c00411

Author Contributions

The manuscript was written through the contributions of all authors. All authors have given approval to the final version of the manuscript. S.T. and O.K.K. contributed equally.

Notes

The authors declare no competing financial interest.

ACKNOWLEDGMENTS

S.T., an early stage researcher within the NANOMED project, acknowledges the funding received from the European Union's Horizon 2020 research and innovation program Marie Skłodowska-Curie Innovative Training Networks (ITN) (grant 676137). SPR and proteomics studies were funded through grants from the Instrumentarium Science Foundation, Inkeri and Mauri Vänskä Foundation, and Drug Research Program Joint Grant. A.S. received support from the Lundbeck Foundation (grant R181-2014-3577) and A.U. from the Academy of Finland (grant 311122). The authors also acknowledge the funding received from Santen Oy. The Light Microscopy Unit of the Institute of Biotechnology at the University of Helsinki is thanked for help with confocal microscopy. M.Sc. Marja Hagström is thanked for assistance in proteomics sample preparation.

REFERENCES

(1) del Amo, E. M.; Rimpelä, A.-K.; Heikkinen, E.; Kari, O. K.; Ramsay, E.; Lajunen, T.; Schmitt, M.; Pelkonen, L.; Bhattacharya, M.; Richardson, D.; Subrizi, A.; Turunen, T.; Reinisalo, M.; Itkonen, J.; Toropainen, E.; Casteleijn, M.; Kidron, H.; Antopolsky, M.; Vellonen, K.-S.; Ruponen, M.; Urtti, A. Pharmacokinetic Aspects of Retinal Drug Delivery. *Prog. Retinal Eye Res.* **2017**, *57*, 134−185.

(2) Le Goff, M. M.; Bishop, P. N. Adult Vitreous Structure and Postnatal Changes. *Eye* **2008**, *22* (10), 1214−1222.

(3) Käsdorf, B. T.; Arends, F.; Lieleg, O. Diffusion Regulation in the Vitreous Humor. *Biophys. J.* **2015**, *109* (10), 2171−2181.

(4) Pitkänen, L.; Ruponen, M.; Nieminen, J.; Urtti, A. Vitreous Is a Barrier in Nonviral Gene Transfer by Cationic Lipids and Polymers. *Pharm. Res.* **2003**, *20* (4), 576−583.

(5) Peeters, L.; Sanders, N. N.; Braeckmans, K.; Boussery, K.; Voorde, J. V. de; Smedt, S. C. D.; Demeester, J. Vitreous: A Barrier to Nonviral Ocular Gene Therapy. *Invest. Ophthalmol. Visual Sci.* **2005**, *46* (10), 3553−3561.

(6) Xu, Q.; Boylan, N. J.; Suk, J. S.; Wang, Y.-Y.; Nance, E. A.; Yang, J.-C.; McDonnell, P. J.; Cone, R. A.; Duh, E. J.; Hanes, J. Nanoparticle Diffusion in, and Microrheology of, the Bovine Vitreous Ex Vivo. *J. Controlled Release* **2013**, *167* (1), 76−84.

(7) Martens, T. F.; Vercauteren, D.; Forier, K.; Deschout, H.; Remaut, K.; Paesen, R.; Ameloot, M.; Engbersen, J. F.; Demeester, J.; De Smedt, S. C.; Braeckmans, K. Measuring the Intravitreal Mobility of Nanomedicines with Single-Particle Tracking Microscopy. *Nanomedicine* **2013**, *8* (12), 1955−1968.

(8) Fuchs, H.; Igney, F. Binding to Ocular Albumin as a Half-Life Extension Principle for Intravitreally Injected Drugs: Evidence from Mechanistic Rat and Rabbit Studies. *J. Ocul. Pharmacol. Ther.* **2017**, *33* (2), 115−122.

(9) Rimpelä, A.-K.; Reunanen, S.; Hagström, M.; Kidron, H.; Urtti, A. Binding of Small Molecule Drugs to Porcine Vitreous Humor. *Mol. Pharmaceutics* **2018**, *15* (6), 2174−2179.

(10) Lazarovits, J.; Sindhwani, S.; Tavares, A. J.; Zhang, Y.; Song, F.; Audet, J.; Krieger, J. R.; Syed, A. M.; Stordy, B.; Chan, W. C. W. Supervised Learning and Mass Spectrometry Predicts the in Vivo Fate of Nanomaterials. *ACS Nano* **2019**, *13* (7), 8023−8034.

(11) Ahmad, M. T.; Zhang, P.; Dufresne, C.; Ferrucci, L.; Semba, R. D. The Human Eye Proteome Project: Updates on an Emerging Proteome. *Proteomics* **2018**, *18* (5−6), 1700394.
(12) D'Mello, S. R.; Cruz, C. N.; Chen, M.-L.; Kapoor, M.; Lee, S. L.; Tyner, K. M. The Evolving Landscape of Drug Products Containing Nanomaterials in the United States. *Nat. Nanotechnol.* **2017**, *12* (6), 523−529.
(13) Lajunen, T.; Kontturi, L.-S.; Viitala, L.; Manna, M.; Cramariuc, O.; Róg, T.; Bunker, A.; Laaksonen, T.; Viitala, T.; Murtomäki, L.; Urtti, A. Indocyanine Green-Loaded Liposomes for Light-Triggered Drug Release. *Mol. Pharmaceutics* **2016**, *13* (6), 2095−2107.
(14) Lajunen, T.; Nurmi, R.; Kontturi, L.; Viitala, L.; Yliperttula, M.; Murtomäki, L.; Urtti, A. Light Activated Liposomes: Functionality and Prospects in Ocular Drug Delivery. *J. Controlled Release* **2016**, *244* (Pt B), 157−166.
(15) Kari, O. K.; Ndika, J.; Parkkila, P.; Louna, A.; Lajunen, T.; Puustinen, A.; Viitala, T.; Alenius, H.; Urtti, A. In Situ Analysis of Liposome Hard and Soft Protein Corona Structure and Composition in a Single Label-Free Workflow. *Nanoscale* **2020**, *12* (3), 1728−1741.
(16) Garbuzenko, O.; Barenholz, Y.; Priev, A. Effect of Grafted PEG on Liposome Size and on Compressibility and Packing of Lipid Bilayer. *Chem. Phys. Lipids* **2005**, *135* (2), 117−129.
(17) Stepniewski, M.; Pasenkiewicz-Gierula, M.; Róg, T.; Danne, R.; Orlowski, A.; Karttunen, M.; Urtti, A.; Yliperttula, M.; Vuorimaa, E.; Bunker, A. Study of PEGylated Lipid Layers as a Model for PEGylated Liposome Surfaces: Molecular Dynamics Simulation and Langmuir Monolayer Studies. *Langmuir* **2011**, *27* (12), 7788−7798.
(18) Lajunen, T.; Nurmi, R.; Wilbie, D.; Ruoslahti, T.; Johansson, N. G.; Korhonen, O.; Rog, T.; Bunker, A.; Ruponen, M.; Urtti, A. The Effect of Light Sensitizer Localization on the Stability of Indocyanine Green Liposomes. *J. Controlled Release* **2018**, *284*, 213−223.
(19) Tarantino, N.; Tinevez, J.-Y.; Crowell, E. F.; Boisson, B.; Henriques, R.; Mhlanga, M.; Agou, F.; Israël, A.; Laplantine, E. TNF and IL-1 Exhibit Distinct Ubiquitin Requirements for Inducing NEMO−IKK Supramolecular Structures. *J. Cell Biol.* **2014**, *204* (2), 231−245.
(20) Ribeiro, L. N. de M.; Couto, V. M.; Fraceto, L. F.; Paula, E. de Use of Nanoparticle Concentration as a Tool to Understand the Structural Properties of Colloids. *Sci. Rep.* **2018**, *8* (1), 1−8.
(21) Jung, L. S.; Campbell, C. T.; Chinowsky, T. M.; Mar, M. N.; Yee, S. S. Quantitative Interpretation of the Response of Surface Plasmon Resonance Sensors to Adsorbed Films. *Langmuir* **1998**, *14* (19), 5636−5648.
(22) Rupert, D. L. M.; Shelke, G. V.; Emilsson, G.; Claudio, V.; Block, S.; Lässer, C.; Dahlin, A.; Lötvall, J. O.; Bally, M.; Zhdanov, V. P.; Höök, F. Dual-Wavelength Surface Plasmon Resonance for Determining the Size and Concentration of Sub-Populations of Extracellular Vesicles. *Anal. Chem.* **2016**, *88* (20), 9980−9988.
(23) Vörös, J. The Density and Refractive Index of Adsorbing Protein Layers. *Biophys. J.* **2004**, *87* (1), 553−561.
(24) Cox, J.; Hein, M. Y.; Luber, C. A.; Paron, I.; Nagaraj, N.; Mann, M. Accurate Proteome-Wide Label-Free Quantification by Delayed Normalization and Maximal Peptide Ratio Extraction, Termed MaxLFQ. *Mol. Cell. Proteomics* **2014**, *13* (9), 2513−2526.
(25) Tyanova, S.; Temu, T.; Sinitcyn, P.; Carlson, A.; Hein, M. Y.; Geiger, T.; Mann, M.; Cox, J. The Perseus Computational Platform for Comprehensive Analysis of (Prote)Omics Data. *Nat. Methods* **2016**, *13* (9), 731−740.
(26) Semba, R. D.; Enghild, J. J.; Venkatraman, V.; Dyrlund, T. F.; Van Eyk, J. E. The Human Eye Proteome Project: Perspectives on an Emerging Proteome. *Proteomics* **2013**, *13* (16), 2500−2511.
(27) Aretz, S.; Krohne, T. U.; Kammerer, K.; Warnken, U.; Hotz-Wagenblatt, A.; Bergmann, M.; Stanzel, B. V.; Kempf, T.; Holz, F. G.; Schnölzer, M.; Kopitz, J. In-Depth Mass Spectrometric Mapping of the Human Vitreous Proteome. *Proteome Sci.* **2013**, *11*, 22.
(28) Yee, K. M. P.; Feener, E. P.; Madigan, M.; Jackson, N. J.; Gao, B.-B.; Ross-Cisneros, F. N.; Provis, J.; Aiello, L. P.; Sadun, A. A.; Sebag, J. Proteomic Analysis of Embryonic and Young Human Vitreous. *Invest. Ophthalmol. Visual Sci.* **2015**, *56* (12), 7036−7042.
(29) Skeie, J. M.; Roybal, C. N.; Mahajan, V. B. Proteomic Insight into the Molecular Function of the Vitreous. *PLoS One* **2015**, *10* (5), e0127567.
(30) Jo, D. H.; Kim, J. H.; Son, J. G.; Dan, K. S.; Song, S. H.; Lee, T. G.; Kim, J. H. Nanoparticle-Protein Complexes Mimicking Corona Formation in Ocular Environment. *Biomaterials* **2016**, *109*, 23−31.
(31) Liu, Y.; Bouhenni, R. A.; Dufresne, C. P.; Semba, R. D.; Edward, D. P. Differential Expression of Vitreous Proteins in Young and Mature New Zealand White Rabbits. *PLoS One* **2016**, *11* (4), e0153560.
(32) Skeie, J. M.; Mahajan, V. B. Proteomic Interactions in the Mouse Vitreous-Retina Complex. *PLoS One* **2013**, *8* (11), e82140.
(33) Kyte, J.; Doolittle, R. F. A Simple Method for Displaying the Hydropathic Character of a Protein. *J. Mol. Biol.* **1982**, *157* (1), 105−132.
(34) Walkey, C. D.; Chan, W. C. W. Understanding and Controlling the Interaction of Nanomaterials with Proteins in a Physiological Environment. *Chem. Soc. Rev.* **2012**, *41* (7), 2780−2799.
(35) Noulas, A. V.; Theocharis, A. D.; Feretis, E.; Papageorgakopoulou, N.; Karamanos, N. K.; Theocharis, D. A. Pig Vitreous Gel: Macromolecular Composition with Particular Reference to Hyaluronan-Binding Proteoglycans. *Biochimie* **2002**, *84* (4), 295−302.
(36) Chen, C.-H.; Chen, S. C. Studies on Soluble Proteins of Vitreous in Experimental Animals. *Exp. Eye Res.* **1981**, *32* (4), 381−388.
(37) Kleinberg, T. T.; Tzekov, R. T.; Stein, L.; Ravi, N.; Kaushal, S. Vitreous Substitutes: A Comprehensive Review. *Surv. Ophthalmol.* **2011**, *56* (4), 300−323.
(38) Loukovaara, S.; Nurkkala, H.; Tamene, F.; Gucciardo, E.; Liu, X.; Repo, P.; Lehti, K.; Varjosalo, M. Quantitative Proteomics Analysis of Vitreous Humor from Diabetic Retinopathy Patients. *J. Proteome Res.* **2015**, *14* (12), 5131−5143.
(39) Theocharis, A. D.; Papageorgakopoulou, N.; Feretis, E.; Theocharis, D. A. Occurrence and Structural Characterization of Versican-like Proteoglycan in Human Vitreous. *Biochimie* **2002**, *84* (12), 1235−1241.
(40) Swindle, K. E.; Hamilton, P. D.; Ravi, N. In Situ Formation of Hydrogels as Vitreous Substitutes: Viscoelastic Comparison to Porcine Vitreous. *J. Biomed. Mater. Res., Part A* **2008**, *87A* (3), 656−665.
(41) Kristensen, K.; Engel, T. B.; Stensballe, A.; Simonsen, J. B.; Andresen, T. L. The Hard Protein Corona of Stealth Liposomes Is Sparse. *J. Controlled Release* **2019**, *307*, 1−15.
(42) Hadjidemetriou, M.; McAdam, S.; Garner, G.; Thackeray, C.; Knight, D.; Smith, D.; Al-Ahmady, Z.; Mazza, M.; Rogan, J.; Clamp, A.; Kostarelos, K. The Human In Vivo Biomolecule Corona onto PEGylated Liposomes: A Proof-of-Concept Clinical Study. *Adv. Mater.* **2019**, *31* (4), 1803335.
(43) Kokkinopoulou, M.; Simon, J.; Landfester, K.; Mailänder, V.; Lieberwirth, I. Visualization of the Protein Corona: Towards a Biomolecular Understanding of Nanoparticle-Cell-Interactions. *Nanoscale* **2017**, *9* (25), 8858−8870.
(44) Conway, M. D.; Jermak, C. M.; Peyman, G. A.; Swanson, H. T.; Blake, D. A. Buffering Capacity of Bovine Vitreous. *Retina* **2008**, *28* (1), 150.
(45) Patel, S.; Müller, G.; Stracke, J. O.; Altenburger, U.; Mahler, H.-C.; Jere, D. Evaluation of Protein Drug Stability with Vitreous Humor in a Novel Ex-Vivo Intraocular Model. *Eur. J. Pharm. Biopharm.* **2015**, *95*, 407−417.
(46) Bhattacharjee, S. DLS and Zeta Potential − What They Are and What They Are Not? *J. Controlled Release* **2016**, *235*, 337−351.
(47) Ogawa, K. Scanning Electron Microscopic Study of Hyalocytes in the Guinea Pig Eye. *Arch. Histol. Cytol.* **2002**, *65* (3), 263−268.
(48) Sebag, J. *Imaging Vitreous*; Nature Publishing Group, 2002; pp 429−439.
(49) Triantafilou, M.; Triantafilou, K. Heat-Shock Protein 70 and Heat-Shock Protein 90 Associate with Toll-like Receptor 4 in

Response to Bacterial Lipopolysaccharide. *Biochem. Soc. Trans.* **2004**, *32* (4), 636−639.
(50) Calderwood, S. K.; Gong, J.; Murshid, A. Extracellular HSPs: The Complicated Roles of Extracellular HSPs in Immunity. *Front. Immunol.* **2016**, *7*, 1 DOI: 10.3389/fimmu.2016.00159.
(51) Missel, P. J.; Sarangapani, R. Physiologically Based Ocular Pharmacokinetic Modeling Using Computational Methods. *Drug Discovery Today* **2019**, *24* (8), 1551−1563.
(52) Hutton-Smith, L. A.; Gaffney, E. A.; Byrne, H. M.; Maini, P. K.; Schwab, D.; Mazer, N. A. A Mechanistic Model of the Intravitreal Pharmacokinetics of Large Molecules and the Pharmacodynamic Suppression of Ocular Vascular Endothelial Growth Factor Levels by Ranibizumab in Patients with Neovascular Age-Related Macular Degeneration. *Mol. Pharmaceutics* **2016**, *13* (9), 2941−2950.
(53) Zhou, X.; Xie, J.; Shen, M.; Wang, J.; Jiang, L.; Qu, J.; Lu, F. Biometric Measurement of the Mouse Eye Using Optical Coherence Tomography with Focal Plane Advancement. *Vision Res.* **2008**, *48* (9), 1137−1143.
(54) Krohne, T. U.; Eter, N.; Holz, F. G.; Meyer, C. H. Intraocular Pharmacokinetics of Bevacizumab After a Single Intravitreal Injection in Humans. *Am. J. Ophthalmol.* **2008**, *146* (4), 508−512.
(55) Zhu, Q.; Ziemssen, F.; Henke-Fahle, S.; Tatar, O.; Szurman, P.; Aisenbrey, S.; Schneiderhan-Marra, N.; Xu, X.; Grisanti, S. Vitreous Levels of Bevacizumab and Vascular Endothelial Growth Factor-A in Patients with Choroidal Neovascularization. *Ophthalmology* **2008**, *115* (10), 1750−1755.
(56) Bakri, S. J.; Snyder, M. R.; Reid, J. M.; Pulido, J. S.; Singh, R. J. Pharmacokinetics of Intravitreal Bevacizumab (Avastin). *Ophthalmology* **2007**, *114* (5), 855−859.
(57) Nomoto, H.; Shiraga, F.; Kuno, N.; Kimura, E.; Fujii, S.; Shinomiya, K.; Nugent, A. K.; Hirooka, K.; Baba, T. Pharmacokinetics of Bevacizumab after Topical, Subconjunctival, and Intravitreal Administration in Rabbits. *Invest. Ophthalmol. Visual Sci.* **2009**, *50* (10), 4807−4813.
(58) Barza, M.; Stuart, M.; Szoka, F. Effect of Size and Lipid Composition on the Pharmacokinetics of Intravitreal Liposomes. *Invest. Ophthalmol. Vis. Sci.* **1987**, *28* (5), 893−900.
(59) Araie, M.; Maurice, D. M. The Loss of Fluorescein, Fluorescein Glucuronide and Fluorescein Isothiocyanate Dextran from the Vitreous by the Anterior and Retinal Pathways. *Exp. Eye Res.* **1991**, *52* (1), 27−39.
(60) Sebag, J. *Ageing of the Vitreous*; Nature Publishing Group, 1987; pp 254−262.
(61) Christoforidis, J. B.; Williams, M. M.; Wang, J.; Jiang, A.; Pratt, C.; Abdel-Rasoul, M.; Hinkle, G. H.; Knopp, M. V. Anatomic and Pharmacokinetic Properties of Intravitreal Bevacizumab and Ranibizumab after Vitrectomy and Lensectomy. *Retina* **2013**, *33* (5), 946−952.
(62) Ahn, S. J.; Ahn, J.; Park, S.; Kim, H.; Hwang, D. J.; Park, J. H.; Park, J. Y.; Chung, J. Y.; Park, K. H.; Woo, S. J. Intraocular Pharmacokinetics of Ranibizumab in Vitrectomized versus Nonvitrectomized Eyes. *Invest. Ophthalmol. Visual Sci.* **2014**, *55* (1), 567−573.
(63) Niwa, Y.; Kakinoki, M.; Sawada, T.; Wang, X.; Ohji, M. Ranibizumab and Aflibercept: Intraocular Pharmacokinetics and Their Effects on Aqueous VEGF Level in Vitrectomized and Nonvitrectomized Macaque Eyes. *Invest. Ophthalmol. Visual Sci.* **2015**, *56* (11), 6501−6505.

https://dx.doi.org/10.1021/acs.molpharmaceut.0c00411
Mol. Pharmaceutics 2021, 18, 699−713